Topological spin liquids in the ruby lattice with anisotropic Kitaev interactions

Saeed S. Jahromi,[1,*] Mehdi Kargarian,[2] S. Farhad Masoudi,[3] and Abdollah Langari[1,4,†]
[1]*Department of Physics, Sharif University of Technology, Tehran 14588-89694, Iran*
[2]*Condensed Matter Theory Center and Joint Quantum Institute, Department of Physics, University of Maryland, College Park, Maryland 20742, USA*
[3]*Department of Physics, K. N. Toosi University of Technology, Post Office Box 15875-4416, Tehran, Iran*
[4]*Center of Excellence in Complex Systems and Condensed Matter, Sharif University of Technology, Tehran 14588-89694, Iran*
(Received 31 July 2016; published 26 September 2016)

The ruby lattice is a four-valent lattice interpolating between honeycomb and triangular lattices. In this work we investigate the topological spin-liquid phases of a spin Hamiltonian with Kitaev interactions on the ruby lattice using exact diagonalization and perturbative methods. The latter interactions combined with the structure of the lattice yield a model with $\mathbb{Z}_2 \times \mathbb{Z}_2$ gauge symmetry. We mapped out the phase diagram of the model and found gapped and gapless spin-liquid phases. While the low-energy sector of the gapped phase corresponds to the well-known topological color code model on a honeycomb lattice, the low-energy sector of the gapless phases is described by an effective spin model with three-body interactions on a triangular lattice. A gap is opened in the spectrum in small magnetic fields, where we showed that the ground state has a finite topological entanglement entropy. We argue that the gapped phases could be possibly described by exotic excitations, and their corresponding spectrum is richer than the Ising phase of the Kitaev model.

DOI: 10.1103/PhysRevB.94.125145

I. INTRODUCTION

Topological phases of matters have attracted a great deal of attention in recent years due to their novel properties such as topologically protected ground states [1], long-range entanglement [2], and emergent quasiparticles with fractional statistics, i.e., anyons [3–7], which make them a suitable playground for topological quantum computation [8]. Our understanding of topologically ordered phases in an exactly solvable spin model began with the toric code introduced by Kitaev [1]. The ground-state manifold is multiple degenerate depending on the genus of the space where the lattice is embedded, and the excitations carry Abelian statistics. However, the many-body nature of the spin interactions involving four-body terms in the underlying Hamiltonian makes its physical realization challenging. This problem was resolved by Kitaev in his seminal work [7] by introducing a simple nearest-neighbor spin Hamiltonian on the honeycomb lattice. An exact solution based on Majorana representation of spins exists for the model yielding the Kitaev model two quantum spin-liquid phases [see Fig. 2(a) for a schematic representation] with $\mathbb{Z}_2$ topological order: a gapped phase which is continuously connected to the toric code and a gapless phase which can host non-Abelian Ising anyons when the Majorana fermions are gapped out by adding perturbations breaking the time-reversal symmetry. Although the toric model was first aimed at exotic excitations for quantum computations, recent experiments have unveiled the prospect of relevance of the Kitaev interactions in the highly anisotropic magnets on honeycomb lattices such as Na_2IrO_3, Li_2IrO_3 [9–12], and α-$RuCl_3$ [13].

The discovery of such quantum magnets presaged the study of other models with anisotropic interactions on different lattices, including decorated honeycomb [14], triangular [15,16], spin ladder [17,18], and ruby [19,20] lattices. The latter one, the ruby color code (RCC) shown in Fig. 1, is central to our work in this paper. The bismuth ions in layered materials such as $Bi_{14}Rh_3I_9$ form a bilayer ruby lattice [21–23] with interesting topological properties. We explore the phase diagram of a spin model with Kitaev interactions (1) on the ruby lattice in terms of exchange couplings (J_x, J_y, J_z) restricted to the plane $J_x + J_y + J_z = 2J$. Anisotropic interactions can in principle arise in transition-metal compounds with strong spin-orbit couplings, which make the superexchange processes highly anisotropic and bond dependent [24].

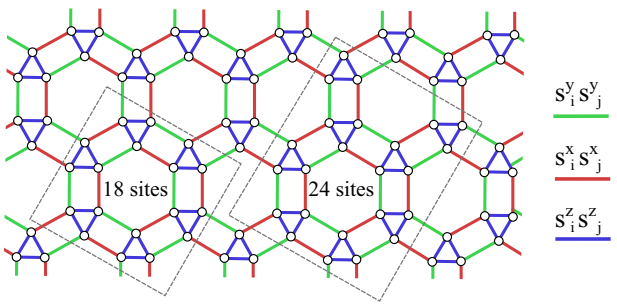

FIG. 1. Ruby lattice Λ of the two-body color code. Spin-1/2 particles are placed on the vertices of the lattice and the spin-spin interactions are denoted by colored links. The rectangular dashed regions further represent the clusters used for exact diagonalization.

When $J_z \gg J_x, J_y$, the low-energy spectrum of the spin model (1) is gapped and the ground-state manifold is topologically ordered [19,20]. The low-energy sector is continuously connected to the so-called topological color code (TCC) model first introduced by Bombin *et al.* [25] to implement the Clifford group, transversally. In contrast to the Kitaev model, the topological order in TCC is associated with $\mathbb{Z}_2 \times \mathbb{Z}_2$ gauge symmetry. This symmetry gives rise to emergence of highly

*jahromi@physics.sharif.edu
†langari@sharif.edu

interacting fermions with semionic mutual statistics in the gapped phase [19].

In this paper, we explore the full phase diagram of the RCC model, which to our best knowledge has not been explored so far. We contrast the phase diagram of $\mathbb{Z}_2 \times \mathbb{Z}_2$ RCC with that of the $\mathbb{Z}_2$ Kitaev model; see Figs. 2(a) and 2(b). We used finite-size exact diagonalization (ED) based on the Lanczos algorithm on periodic clusters of different sizes to map out the full phase diagram of the RCC model from analysis of the ground-state energy and its derivatives. Our results show that the phase diagram contains one gapped and two gapless phases. The gapped phase corresponds to TCC on the honeycomb lattice as mentioned above. The gapless phases appear at the corner of the phase diagram in the regime where either $J_x \gg J_z, J_y$ or $J_y \gg J_z, J_x$. This allows us to use degenerate perturbation theory (DPT) to derive the low-energy effective theory of the underlying phases. We find that the gapless phases are described by an effective Hamiltonian with three-body interactions on a triangular lattice. We argue that the latter phases could be possibly described by a rich structure of Ising anyons due to the underlying $\mathbb{Z}_2 \times \mathbb{Z}_2$ gauge symmetry.

The paper is organized as follows: In Sec. II we introduce the RCC model and review some of the features of the model used in the paper. We present the phase diagram of the model in Sec. III and characterize the underlying phases emerging in different coupling regimes of the problem in Sec. IV. A possible description of phases in terms of Ising anyons is discussed in Sec. V.

II. THE MODEL

The RCC model [19] is a quantum spin system defined on a certain type of four-valent graphs, i.e., the ruby lattice Λ shown in Fig. 1. The model is constructed by placing the spin-1/2 degrees of freedom on vertices of the lattice and inducing two-body interactions of different types, distinguished by colored links, between nearest neighbors. The Hamiltonian of the RCC model is then defined as

$$H = -\sum_{\alpha=x,y,z} J_\alpha \sum_{\alpha-\text{links}} s_i^\alpha s_j^\alpha, \tag{1}$$

where the first sum runs over α links ($\alpha = x, y, z$) labeled by red (r), green (g), and blue (b) colors, respectively, and the second sum runs over the two-body interactions acting on sites i and j of the α links, and s^α stands for Pauli matrices. Here, we set $J_\alpha > 0$. The RCC model supports loop structures as well as string-net integrals of motions defined by connecting certain vertices and links of the lattice, underlying a $\mathbb{Z}_2 \times \mathbb{Z}_2$ gauge symmetry [20].

In contrast to the Kitaev honeycomb model [7], the two-body color code on the ruby lattice is not exactly solvable because of the four-valence structure (four bonds are emanating from each site) of the lattice as opposed to the three-valence structure of the honeycomb lattice. Therefore, we resort to numerical techniques and approximation methods to map out the phase diagram of the Hamiltonian (1) in different coupling regimes (J_x, J_y, J_z). We restrict the exchange coupling to the $J_x + J_y + J_z = 2J$. The coupling J accounts for an overall energy scale, which we set to be unit $J = 1$ throughout.

III. PHASE DIAGRAM

We apply the exact diagonalization technique to the Hamiltonian (1) to capture the possible phases and phase transitions in different coupling regimes, by analyzing the ground-state energy of the system and its derivatives. Our ED algorithm relies on the Lanczos method on the periodic clusters with 18 and 24 sites shown in Fig. 1. Matrix elements of the Hamiltonian are further generated using the s^z Pauli vector space and bit representation.

In order to capture the phase transitions of the model, we have calculated the second derivative of the ground-state energy per site (SDE) in the $J_x + J_y + J_z = 2$ plane and detected the phase boundaries from the diverging behavior of the second derivatives of the energy as shown in Fig. 2(c). Due to the finite-size lattices, a real divergence is obscured. Thus, we take the location of the minimum of SDE as a phase transition point. This might be a crude estimation of locating the phase transition, but we notice that on the paths in the phase diagram with possible phase transitions, e.g., the dashed red line in Fig. 2(b), the behavior of SDE significantly differs from those paths with no phase transition. Moreover, moving from a lattice with 18 sites to a larger one with 24 sites, the minima in SDE become slightly deeper providing a strong evidence of phase transition. We elaborate on details on such transitions below.

To find the phase boundaries we look for the minima in SDE along paths corresponding to the intersection of the plane $J_x + J_y + J_z = 2$ with a plane at fixed J_z $(0 < J_z < 2)$. We use J_s accounting for a one-dimensional parameter space referring to the points lying on the intersection line. A few of such lines are shown as dashed lines in Fig. 2(b), where we show the full phase diagram of the RCC model. We begin by setting $J_z = 0.1$, the dashed green line. The corresponding SDE is plotted in Fig. 2(c) with the same color to make the comparison with other SDE's easier. As seen, only one phase transition is signaled at $(J_x = 0.95, J_y = 0.95, J_z = 0.1)$. Increasing J_z further, we did not observe other phase transitions until a multicritical point at $\mathbf{J}_c \approx (0.85, 0.85, 0.3)$ is reached, beyond which there are multiple phase transitions. We sum up this part by concluding that the region of the phase diagram with $0 < J_z < 0.3$ has two phases which we label as A_2 and A_3. The phase transition in this region occurs when $J_x = J_y$.

Now we move the parameter line J_s to go beyond the $\mathbf{J}_c \approx (0.85, 0.85, 0.3)$ point in the phase diagram, e.g., the dashed red and blue lines in Fig. 2(b). Increasing $J_z > 0.3$, we observe that two distinct minima start to appear in the SDE curves. For instance let us consider the behavior of SDE as the parameter J_s varies on the dashed red line in Fig. 2(b). On this particular line $J_z = 0.5$. We observed that two minima appeared in SDE. The first minimum signals a phase transition out of the A_2 phase to another phase that we call A_1, and the second minimum signals yet another phase transition from A_1 phase to A_3 phase. For J_z's in the interval $0.3 < J_z < 0.69$ two minima appeared in SDE's, making phase boundaries between different phases marked by squares in Fig. 2(b). Moving beyond the $J_z > 0.69$, no phase transition appears, which shows that the RCC model is in the A_1 phase in this part of the phase diagram. Consider a parameter line J_s corresponding to the dashed blue line $J_z = 0.9$ on the phase diagram. The SDE plot is free of any

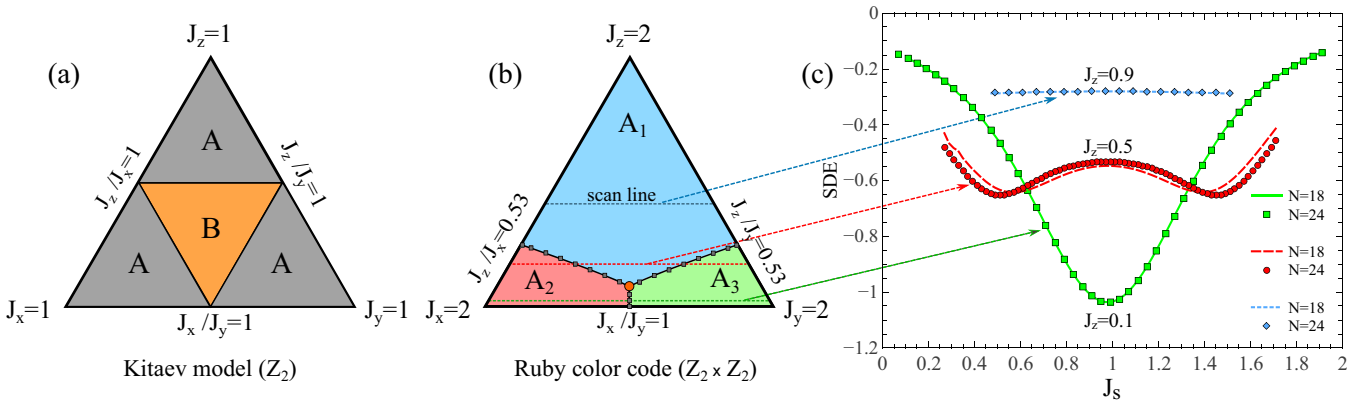

FIG. 2. Phase diagrams of (a) the Kitaev model [7] in the $J_x + J_y + J_z = 1$ plane and (b) the ruby color code model in Eq. (1) in the $J_x + J_y + J_z = 2$ plane studied in this paper. The Kitaev model has the following phases: three symmetry-related gapped phases denoted by phase A, the low-energy description of which is given by the toric code model and the gapless phase B, which becomes a gapped phase with non-Abelian Ising anyons upon breaking time-reversal symmetry. On the other hand the phase diagram of the RCC model consists of three phases labeled as A_1, A_2, A_3. The A_1 phase is a topological gapped phase, and two symmetry-related gapless A_2 and A_3 phases. The phase boundaries are signaled by diverging, up to finite-size effects, of the second derivative of the ground-state energy per site, obtained by ED on periodic clusters with 18 and 24 sites. In (c) we show a few of them each corresponds to the line $J_x + J_y = 2 - J_z$ for a fixed J_z. We show this line by J_s.

minimum leading us to a conclusion that there is no more phase transition.

IV. LOW-ENERGY DESCRIPTION OF PHASES

The analysis presented in the preceding section yields a phase diagram with three distinct phases for the RCC model (1) within ED on finite clusters. According to the phase diagram Fig. 2(b), each phase emerges when one of the couplings of the Hamiltonian is stronger than the two others. For example, the A_1 phase corresponds to the $J_z \gg J_x, J_y$ coupling regime with strong interaction on the blue links, while the A_2 (A_3) phase emerges in the $J_x \gg J_y, J_z$ ($J_y \gg J_y, J_z$) coupling regime with strong interaction on the red (green) links. Symmetry of the lattice structure further imposes that A_2 and A_3 phases be equivalent, up to the interchange of the couplings ($J_y \leftrightarrow J_x$) and colors of the red and green links. Here, we elaborate on the properties of the phases by focusing on each regime.

A. Topological color code: A_1 gapped phase

The A_1 phase arises in the particular regime of the couplings where $J_z \gg J_x, J_y$. This regime of the problem has already been studied in detail in Refs. [19,20] and it has been shown that the low-energy physics of the Hamiltonian (1) in this limit is described by an effective topological color code model [25] on the honeycomb lattice; see Figs. 3(a)–3(c). The low-energy description in this limit is given by a many-body Hamiltonian as follows:

$$H_{\mathrm{TCC}} = -\sum_{p} (\tilde{J}_z Z_p + \tilde{J}_x X_p + \tilde{J}_y Y_p), \qquad (2)$$

where the sum runs over hexagonal plaquettes and the plaquette operators are the product of Pauli matrices around a hexagon $Z_p = \prod_{i\in p} s_i^z$ and $X_p = \prod_{i\in p} s_i^x$ and $Y_p = \prod_{i\in p} s_i^y$. The coupling $\tilde{J}_z$ arises at sixth order of degenerate perturbation theory, while $\tilde{J}_x$ and $\tilde{J}_y$ arise at ninth order [20]. The ground state of the model (2) is separated from the excited state by a gap. For a lattice with periodic boundary conditions defined on a torus with genus $g = 1$ the ground-state manifold is 16-fold degenerate resulting from the $\mathbb{Z}_2 \times \mathbb{Z}_2$ gauge symmetry, as opposed to fourfold degeneracy of the toric code with a $\mathbb{Z}_2$ gauge group symmetry. Recently, a minimal TCC with seven qubits has been simulated in optical lattices being capable of detecting and correcting the errors [26]. The model has been the subject of several studies and many features of the model have already been revealed, ranging from error threshold [27], robustness [28–30], entanglement properties [31], and interesting quasiparticle excitations [32].

B. Effective low-energy description of A_2 and A_3 phases

The nature of the A_2 phase and low-energy physics of the Hamiltonian (1) in the limit $J_x \gg J_y, J_z$, to the best of our knowledge, is not *a priori* known. A similar limit for the Kitaev model on the honeycomb lattice has already been studied in Refs. [33,34]. As discussed above, the phase A_3 arises in the limit $J_y \gg J_x, J_z$. Thus, we need to study one of them. We argue how the ruby lattice in the isolated-dimer limit is connected to a triangular lattice, and we set up a perturbative picture in the low-energy sector of the RCC model based on degenerate perturbation theory which is applied directly to the ($J_x \gg J_y, J_z$) limit of the Hamiltonian (1).

The ruby lattice in the isolated-dimer limit is connected to a triangular lattice as shown in Figs. 3(d)–3(f). This is best perceived by coloring the hexagons and the rectangles of the ruby lattice such that each rectangle connects two hexagons of the same color in the long direction and shares the same color with the hexagons. Following such coloring rules, the resulting colored ruby lattice is illustrated in Fig. 3(e). Next we replace the red links of the ruby lattice by red sites which shrink the hexagons and rectangles of the ruby lattice into *down* and *up* triangles labeled by $\bigtriangledown_c$ and $\bigtriangleup_c$, respectively [see Fig. 3(g)]. The subscript $c \in \{\mathrm{r},\mathrm{b},\mathrm{g}\}$ denotes the color of

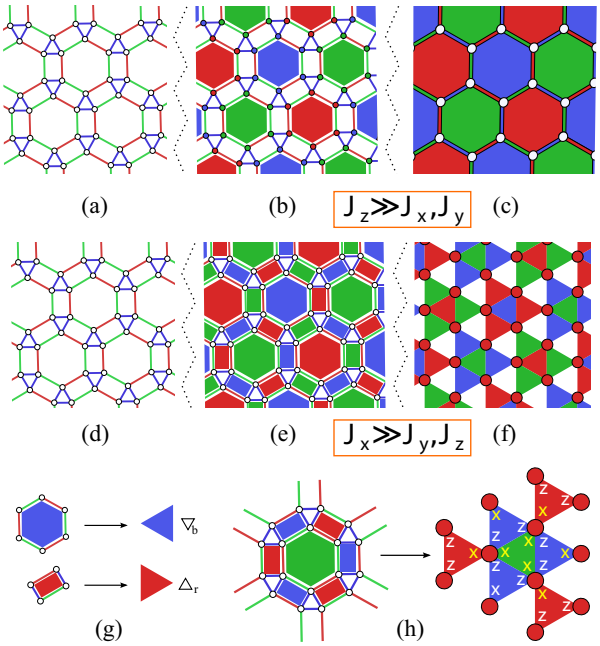

FIG. 3. The connection between the original ruby lattice and effective honeycomb (a–c) and triangular (d–f) lattices corresponding to shrinking of blue triangles and red links to sites v. These limits, in the degenerate perturbation theory, correspond to $J_z \gg J_x, J_y$ and $J_x \gg J_z, J_y$ yielding effective Hamiltonians (2) and (6), respectively. (g) Examples of the transformation of a blue hexagon and red rectangle to down triangle ∇_b and up triangle $\triangle_r$, respectively. (h) A ruby plaquette and its corresponding triangular cluster in the effective language. The plaquette spin operators appearing in Hamiltonian (6) are further shown by notations $x \equiv \tau^x$ and $z \equiv \tau^z$.

the reduced triangles. The ruby lattice is then reduced to a triangular lattice labeled by $\tilde{\Lambda}$; see Fig. 3(f).

Next we use degenerate perturbation theory in the limit $J_x \gg J_y, J_z$ to derive an effective model on the triangular lattice $\tilde{\Lambda}$. Before that, let us for simplicity rotate the Hamiltonian (1) such that $(s^x, s^y, s^z) \to (s^z, s^y, -s^x)$ and then write it in the form $H = H_0 + V$ where H_0 is the unperturbed diagonal part and V is the perturbation represented by

$$H_0 = -J_x \sum_{\text{r-link}} s_i^z s_j^z, \tag{3}$$

$$V = -J_y \sum_{\text{g-link}} s_i^y s_j^y - J_z \sum_{\text{b-link}} s_i^x s_j^x, \tag{4}$$

where i, j denote the nearest neighbors on the bonds of the ruby lattice. In the extreme case where $J_y, J_z = 0$, the system is composed of isolated red dimers, where its ground state is given by $|\uparrow\uparrow\rangle$ and $|\downarrow\downarrow\rangle$ ferromagnetic states on the red links. The ground state of the system is therefore 2^{N_d}-fold degenerate (where $N_d = N/2$ is the number of red dimers) with ground-state energy $E_0 = -N_d J_x$. Excitations of the model correspond to antiferromagnetic red dimers that each cost $2J_x$, i.e., the first excited state of the system is $2N_d \times 2^{N_d - 1}$-fold degenerate and has a total energy $E_1 = E_0 + 2J_x$. Effects of $J_y, J_z \neq 0$ interactions can further be studied perturbatively, around the strong J_x couplings.

As we pointed out, the red dimers of the ruby lattice are equivalent to the vertices of the effective triangular lattice $\tilde{\Lambda}$. We therefore label each dimer by an index v and define a projection operator on each dimer:

$$P_v = |\Uparrow\rangle\langle\uparrow\uparrow| + |\Downarrow\rangle\langle\downarrow\downarrow|, \tag{5}$$

where $|\Uparrow\rangle$ and $|\Downarrow\rangle$ are effective spin-1/2 on the vertex v of lattice $\tilde{\Lambda}$. The ground state of H_0 is massively degenerate, and a weak perturbation V lifts the degeneracy substantially. The low-energy sector then can be described by an effective Hamiltonian arising at the third order of perturbation. The details of the calculation are given in Appendix A. The effective Hamiltonian reads as

$$H_{\text{eff}}^{(3)} = e_0 + J_\nabla \sum_{\nabla \in \tilde{\Lambda}} \mathcal{A}_\nabla + J_\triangle \sum_{\triangle \in \tilde{\Lambda}} \mathcal{B}_\triangle \tag{6}$$

where

$$\frac{e_0}{N} = -\frac{1}{2} - \frac{J_y^2}{2J_x} - \frac{J_z^2}{J_x} - \frac{J_y^3}{J_x^2}, \tag{7}$$

$$J_\nabla = \frac{3J_y^3}{2J_x^2}, \quad J_\triangle = \frac{3J_y J_z^2}{2J_x^2}, \tag{8}$$

$$\mathcal{A}_\nabla = -\prod_{v \in \nabla} \tau_v^x, \tag{9}$$

$$\mathcal{B}_\triangle = -\prod_{v \in \triangle} \tau_v^w, \quad w = \begin{cases} x, & \text{if } v \in \mathcal{V} \\ z, & \text{if } v \in \mathcal{E} \end{cases}, \tag{10}$$

where τ_v^α ($\alpha = x, z$) are the pseudo-Pauli operators acting on space spanned by $|\Uparrow\rangle$ and $|\Downarrow\rangle$ states. On the triangular lattice $\tilde{\Lambda}$, each ∇_c triangle is surrounded by three $\triangle_{\bar{c}}$ triangles and shares three edges with them and is further connected to three $\triangle_{\bar{\bar{c}}}$ triangles through its corners. Here the color changing bar operators are defined as

$$\bar{\text{r}} = \text{g}, \quad \bar{\text{g}} = \text{b}, \quad \bar{\text{b}} = \text{r}. \tag{11}$$

Figure 3(h) illustrates an example of a down triangle ∇_g which shares edges with the three neighboring up triangles $\triangle_b$ and is connected to three other up triangles $\triangle_r$ at its corners. Denoting the group of shared edges (vertices) by $\mathcal{E}$ ($\mathcal{V}$), the structure of the $\mathcal{B}_\triangle$ plaquette operator in Eq. (10) becomes clear.

Other orders of perturbation rather contribute to the ground-state energy as an energy shift or produce terms that are always products of $\mathcal{A}_\nabla$ and $\mathcal{B}_\triangle$ plaquette operators. The overall low-energy effective theory of the RCC in the isolated-dimer limit is therefore given by Eq. (6). Unlike the TCC model, which is exactly solvable, the anticommutation of some plaquette operators appearing in Eq. (6) obscures the exact solution. It is easy to see that $\{\mathcal{B}_\triangle^c, \mathcal{B}_\triangle^{c'}\} = 0$ when triangles share a site. Nevertheless, as shown in Appendix B, the model possess the $\mathbb{Z}_2 \times \mathbb{Z}_2$ gauge symmetry.

We, therefore, numerically explore the energy spectrum of Eq. (6). In the extreme limit where $J_\triangle = 0$, the energy spectrum of H_{eff} is gapped as shown in Fig. 4. The most left pillar of the spectrum clearly shows the large gap between

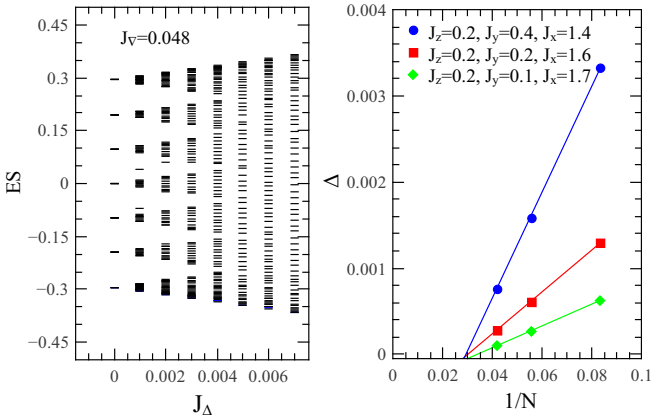

FIG. 4. Left: Energy spectrum of the effective Hamiltonian (6) for $J_\nabla = 0.048$ and varying $J_\triangle$ obtained by ED on periodic triangular clusters with 24 sites. Right: Scaling of the energy gap Δ between the two lowest-energy levels for different couplings in the A_2 phase. The gap approaches zero by increasing the system size, indicating the gapless nature of the A_2 phase.

the degenerate ground states and the excited states of the the effective Hamiltonian (6) at $J_\triangle = 0$. The energy spectrum of the effective Hamiltonian (6) is studied by gradually increasing $J_\triangle$. Surprisingly, even a very small $J_\triangle$ would drastically change the energy spectrum and breaks the degeneracy of the ground state at $J_\triangle = 0$ coupling. Splitting of the energy levels at the bottom of the spectrum for different regimes of $J_\triangle$ is clearly shown in Fig. 4.

In order to determine if the energy spectrum of the A_2 phase is gapped or gapless, we performed scaling over the energy gap between the two lowest eigenstates of the effective Hamiltonian (6) in the $(J_\triangle, J_\nabla \neq 0)$ limits for different system sizes on triangular lattice $\tilde{\Lambda}$ with $N = 12, 18, 24$. The scaling was performed for different $J_\triangle, J_\nabla$ couplings and (J_x, J_y, J_z) were chosen to make sure we are deeply in the A_2 phase (see Fig. 4). Our results certify that the energy gap approaches zero by increasing the system size indicating the gapless nature of the A_2 phase. The same fact holds for the A_3 phase up to the interchange of J_x and J_y couplings.

V. SUMMARY AND OUTLOOK

In this work we used numerical and perturbative methods to map out the phase diagram of the RCC model with $\mathbb{Z}_2 \times \mathbb{Z}_2$ gauge symmetry, and the main results are summarized in Fig. 2(b). We found three distinct phases present in the phase diagram separated from each other by three phase boundaries met at a multicritical point: (i) the A_1 is a gapped phase arising in the strong J_z coupling, the low-energy excitations of which are known to have Abelian statistics, and (ii) the A_2 and A_3 are two gapless phases arising in the regimes of couplings where either J_x or J_y, respectively, is the strongest one. The low-energy descriptions of latter phases are given by a three-body effective Hamiltonian (6) on the triangular lattice.

The latter phases are not continuously connected to a trivial paramagnetic phase in the presence of a magnetic field; see Appendix C for details. Indeed, we found there is a regime where the spectrum becomes gapped in the presence of a magnetic field. This behavior is not dissimilar to the magnetic field-induced gapped phase, the B phase in Fig. 2(a), in the Kitaev honeycomb model [7]. To determine whether the gapped phase is possibly a topologically ordered phase, we evaluated the topological entanglement entropy (TEE). The results are shown in Fig. 7. In contrast to the trivial polarized phase, which gives zero for TEE, the nonzero value of TEE in the gapped phase points to a distinct feature of this phase; the ground state could be topologically ordered.

The exact determination of the nature of excitations in A_2 and A_3 phases is, however, rather elusive due to the lack of the exact solutions of the RCC model (1) and three-body effective interactions (6). However, we present a possible scenario below. We use an analogy with the Abelian and non-Abelian phases of the Kitaev model. The very low-energy description of the former is given by four superselection sectors: the vacuum 1, the magnetic m and electric e particles, and the fermion $\epsilon = e \times m$. The latter phase is described by three superselection sectors: the vacuum 1, the Ising anyons σ, and the fermion ϵ. A connection between Abelian and non-Abelian Ising anyons has already been put forward [35,36]. Especially, it is shown that the σ particles can be identified form a superposition of strings of m and e anyons [35]:

$$|\sigma_1\sigma_2;\pm\rangle = \frac{1}{\sqrt{2}}(|e_1e_2\rangle \pm |m_1m_2\rangle), \tag{12}$$

where e_1 and e_2 are the end points of an open string; the same holds for m_1 and m_2. The $\mathbb{Z}_2 \times \mathbb{Z}_2$ Abelian gapped phase is basically two copies of the toric code model [37–39]. Thus, we expect the same construction can be used to identify the possible Ising anyons in the RCC model. The low-energy sector of the Abelian phase is described by 16 superselection sectors [20,32]: the vacuum 1, the anyons $\{e^{\mathrm{r}}, e^{\mathrm{b}}, e^{\mathrm{g}}, m^{\mathrm{r}}, m^{\mathrm{b}}, m^{\mathrm{g}}\}$, bosons $\{e^{\mathrm{r}} \times m^{\mathrm{r}}, e^{\mathrm{b}} \times m^{\mathrm{b}}, e^{\mathrm{g}} \times m^{\mathrm{g}}\}$, and the fermions $\{e^{\mathrm{r}} \times m^{\mathrm{b}}, e^{\mathrm{r}} \times m^{\mathrm{g}}, e^{\mathrm{b}} \times m^{\mathrm{r}}, e^{\mathrm{b}} \times m^{\mathrm{g}}, e^{\mathrm{g}} \times m^{\mathrm{r}}, e^{\mathrm{g}} \times m^{\mathrm{b}}\}$. Note that $e^{\mathrm{r}} \times e^{\mathrm{b}} \times e^{\mathrm{g}} = 1$ and $m^{\mathrm{r}} \times m^{\mathrm{b}} \times m^{\mathrm{g}} = 1$ due to $\mathbb{Z}_2 \times \mathbb{Z}_2$ symmetry. Superposing the anyonic states, we obtain the Ising anyons as follows:

$$|\sigma_1^c\sigma_2^c;\pm\rangle = \frac{1}{\sqrt{2}}\left(|e_1^{\bar{c}}e_2^{\bar{c}}\rangle \pm |m_1^{\bar{\bar{c}}}m_2^{\bar{\bar{c}}}\rangle\right). \tag{13}$$

This suggests that two classes of colored Ising anyons, due to $\mathbb{Z}_2 \times \mathbb{Z}_2$ symmetry, may arise in the gapless phases of the RCC model upon adding time-reversal breaking perturbations. Therefore, we conjecture that the Abelian A_1 phase undergoes a phase transition to A_2 and A_3 phases with colored Ising anyons σ^c. Viewed the topological color code as two coupled toric code models [37–39], it suggests that the construction (13) could be a spin analog of coupled bilayer fractional quantum Hall states with $\mathbb{Z}_2$ symmetry. It is shown that for latter systems the condensation of Abelian anyons in the layers via a phase transition leads to rich structure for non-Abelian anyons such as Ising $\times \mathbb{Z}_2$ and Ising $\times$ Ising [40,41]. However, understanding the precise connection of this scenario to A_2 and A_3 phases requires more elaborative numerical studies, which can be a subject for future study.

ACKNOWLEDGMENTS

The authors acknowledge Abolhassan Vaezi, Kai P. Schmidt, R. Haghshenas, and H. Yarloo for helpful discussions. S.S.J. and A.L. acknowledge support from the Iran National Science Foundation under Grant No. 93023859 and the Sharif University of Technology's Office of Vice President for Research.

APPENDIX A: DEGENERATE PERTURBATION THEORY

In this section, we study the low-energy physics of the RCC Hamiltonian (1) in the $J_x \gg J_y, J_z$ limit. Considering H_0 [Eq. (3)] as diagonal part of the RCC Hamiltonian, the effect of the remaining parts [Eq. (4)] on H_0 can be studied as perturbation V. As we have pointed out in Sec. IV, H_0 has a highly degenerate ground-state subspace and a weak perturbation can lift the degeneracy substantially. We therefore apply the DPT technique based on the projection operators and Green's-function formalism [42] to extract the low-energy effective theory of the RCC model. Denoting the degenerate ground-state subspace of the diagonal unperturbed part, H_0, by $\mathcal{C}$, the projection of any state $|\Psi\rangle$ to this subspace is given by $|\Psi_0\rangle = \mathcal{P}|\Psi\rangle$ where

$$\mathcal{P} = \prod_v P_v \tag{A1}$$

and P_v, defined in Eq. (5), is the projection from the $|\uparrow\uparrow\rangle, |\downarrow\downarrow\rangle$ physical qubits on sites i, j of a red dimer on the ruby lattice Λ to logical qubits on the vertex v of the effective triangular lattice $\tilde{\Lambda}$. The projected state $|\Psi_0\rangle$ then satisfies the effective Schrödinger equation in a perturbative level

$$\left[E_0 + \mathcal{P}V\sum_{n=0}^{\infty}\mathcal{G}^n\mathcal{P}\right]|\Psi_0\rangle = E|\Psi_0\rangle = H_{\text{eff}}|\Psi_0\rangle, \tag{A2}$$

where $\mathcal{G} = \frac{1}{E-H_0}(1-\mathcal{P})V$. The ground-state energy E can then be expanded in a series in perturbation parameters (J_y, J_z in our case) within the degenerate manifold

$$E = E_0^{(0)} + \sum_{k=1}^{\infty} E_0^{(k)}, \tag{A3}$$

where k is the order of perturbation.

According to the particular form of Eq. (4), the perturbation V would be a product of s^x and s^y Pauli operators, which act on different green and blue bonds of the ruby lattice in different orders of perturbation and take the ground-state subspace to the excited state. However, there are particular configurations of the bonds by acting on which the ground-state subspace is projected to itself, i.e., preserves the ferromagnetic configurations of the dimers.

At zeroth order of perturbation, the effective Hamiltonian is denoted by $H_{\text{eff}}^{(0)} = E_0^{(0)}$. The first-order contribution is given by

$$H_{\text{eff}}^{(1)} = \mathcal{P}V\mathcal{P}. \tag{A4}$$

It is straightforward to check that the action of any two-body perturbation of the form $s_i^w s_j^w$ $(w = x, y)$ on green and blue links excites two red bonds to their antiferromagnetic configurations and takes the system out of its ground-state manifold. Therefore, $\mathcal{P}V\mathcal{P} = 0$ in the first order. In the second order of perturbation, the effective Hamiltonian reads

$$H_{\text{eff}}^{(2)} = \mathcal{P}VSV\mathcal{P}, \tag{A5}$$

where $S = 1/(E_0^{(0)} - H_0)$. The second order consists of two V terms and the only nonzero contribution which keeps the system in its ground-state subspace originates from those processes, wherein the two V terms double touch the blue and green bonds. In other words, the first V excite two red dimers connected by a blue or green link to their excited states and the second V returns them back to their original state. Therefore, in the second order the effective Hamiltonian acts trivially on the ground-state manifold and just shifts the ground-state energy by

$$H_{\text{eff}}^{(2)} = -\frac{J_y^2}{2J_x}N - \frac{J_z^2}{J_x}N, \tag{A6}$$

where N is the number of lattice sites.

Order 3 is by far the most interesting because the first nontrivial terms emerge at this order. The effective Hamiltonian at order 3 is given by

$$H_{\text{eff}}^{(3)} = \mathcal{P}V(SV)^2\mathcal{P}. \tag{A7}$$

There are particular products of green and blue bonds, which map the subspace of the system to itself and break the degeneracy of the ground-state manifold:

$$\prod_{\langle ij\rangle\in \text{g,b}-\text{link}} s_i^w s_j^w, \quad w = x, y. \tag{A8}$$

H_{eff} at the third order contains three V terms which can act in two different ways with nontrivial outcome on the ruby lattice as depicted in Fig. 5. The first nontrivial term emerges from the product of three $s_i^y s_j^y$ on the green bonds of the inner hexagons of a plaquette on the ruby lattice [see Fig. 5(a)]. Such a product shrinks the inner hexagon of a ruby plaquette with color c to a *down* triangle $\triangledown_c$ and encodes a logical $-\tau_v^x$ operator on each vertex v of the $\triangledown_c$ triangle. This can explicitly be seen from the following relation:

$$P_v s_i^y s_j^y P_v = -|\Uparrow\rangle\langle\Downarrow| - |\Downarrow\rangle\langle\Uparrow| = -\tau_v^x, \tag{A9}$$

where P_v is the projector defined in Eq. (5). Therefore, the expression (A8) at order 3 encodes the three-body

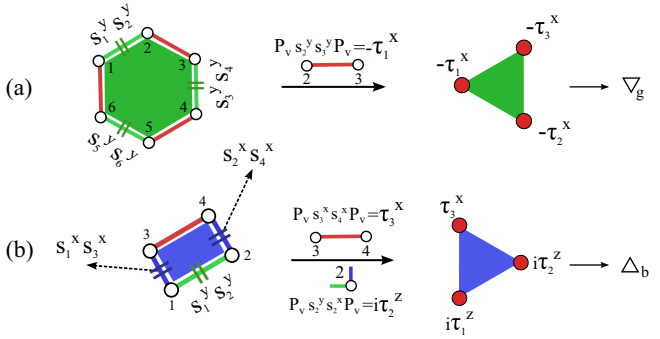

FIG. 5. The pictorial demonstration of the action of H_{eff} in order 3 of perturbation which shrinks the hexagons and rectangles of the ruby lattice to the up and down triangles and encodes effective Pauli operators on the vertices v of the triangles. (a) Emergence of $\triangledown_g$ and (b) $\triangle_b$ triangles and the corresponding plaquette operators.

plaquette operator $\mathcal{A}_\nabla$ (9) on the ∇_c triangles of the lattice $\tilde{\Lambda}$.

The next nontrivial term emerges from the action of two $s_i^x s_j^x$ on blue links and one $s_i^y s_j^y$ on the green bond of the rectangles of the ruby lattice as shown in Fig. 5(b). The action of V then maps the the red dimer of the rectangle to an effective vertex and encodes a logical τ_v^x operator on it. This process further encodes two logical $i\tau_v^z$ operators on the remaining vertices of the rectangle. As a result, the rectangle with color c is reduced to an *up* triangle $\triangle_c$. The projection can be best understood by noting that

$$P_v s_i^x s_i^y P_v = P_v i s_i^z P_v = i|\Uparrow\rangle\langle\Uparrow| - i|\Downarrow\rangle\langle\Downarrow| = i\tau_v^z, \quad \text{(A10)}$$

$$P_v s_i^x s_j^x P_v = |\Uparrow\rangle\langle\Downarrow| + |\Downarrow\rangle\langle\Uparrow| = \tau_v^x. \quad \text{(A11)}$$

These operators all together encode the $\mathcal{B}_\triangle$ plaquette operator (10) acting on the $\triangle_c$ triangles the lattice $\tilde{\Lambda}$.

There is also another term at order 3 which arises from the action of three $s_i^x s_j^x$ on the three connected bonds of a blue triangle on the ruby lattice which has a trivial action on the ground-state subspace and just shifts the ground-state energy. The low-energy spectrum of the system at order 3 of perturbation is then given by Hamiltonian (6).

Similar to order 2, the fourth order also shifts the ground-state energy, trivially. However, starting from order 5, the nontrivial terms which break the degeneracy again start to appear in the ground-state manifold. One can check that these new terms are always the products of $\mathcal{A}_\nabla$ and $\mathcal{B}_\triangle$ plaquette operators. The overall low-energy effective theory of the ruby color code model in the isolated-dimer limit is therefore given by Eq. (6).

APPENDIX B: STRING OPERATORS AND INTEGRALS OF MOTION IN THE A_2 PHASE

In the previous section, we showed that the low-energy physics of the A_2 phase is described by the effective Hamiltonian (6). With a closer look at the model and the effective lattice $\tilde{\Lambda}$ as shown in Fig. 3(f), one can notice that the following commutation relations hold for the $\mathcal{A}_\nabla$ and $\mathcal{B}_\triangle$ plaquette operators:

$$\left[\mathcal{A}_\nabla^c, \mathcal{A}_\nabla^c\right] = \left[\mathcal{A}_\nabla^c, \mathcal{A}_\nabla^{c'}\right] = 0, \quad \text{(B1)}$$

$$\left[\mathcal{A}_\nabla^c, \mathcal{B}_\triangle^c\right] = \left[\mathcal{A}_\nabla^c, \mathcal{B}_\triangle^{c'}\right] = 0, \quad \text{(B2)}$$

$$\left[\mathcal{B}_\triangle^c, \mathcal{B}_\triangle^c\right] = 0, \quad \text{(B3)}$$

$$\left[\mathcal{B}_\triangle^c, \mathcal{B}_\triangle^{c'}\right] = 0 \quad \text{if they share no sites,} \quad \text{(B4)}$$

$$\left\{\mathcal{B}_\triangle^c, \mathcal{B}_\triangle^{c'}\right\} = 0 \quad \text{if they share a site.} \quad \text{(B5)}$$

Due to the latter anticommutation relation, Eq. (B5), the effective Hamiltonian (6) is not exactly solvable. However, the $\mathcal{A}_\nabla$ operator commutes with all terms of the H_{eff} and is therefore the integral of motion (IOM). It is possible to show that the effective model further possesses two other IOMs which can be produced either by the products of certain $\mathcal{A}_\nabla$ and $\mathcal{B}_\triangle$ operators or by going to high orders of perturbation, as will be shown subsequently.

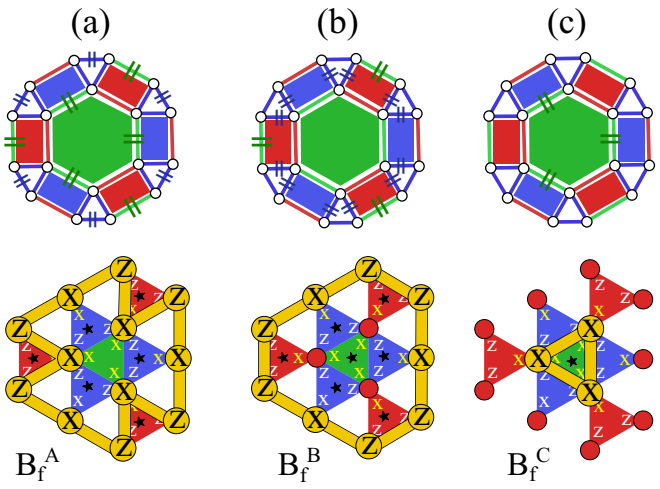

FIG. 6. (a–c) Top: The links which are touched by $s_i^w s_j^w$ ($w = x, y$) interaction in orders 15,12, and 3 with the net effect of producing B_f^A, B_f^B, and B_f^C elementary IOMs on the triangular lattice, respectively. (a–c) Bottom: The effective elementary IOMs on the triangular lattice. The black stars denote the $\mathcal{A}_\nabla, \mathcal{B}_\triangle$ operators, which their product contributes in the structure of the elementary IOM operators.

The second IOM of the model emerges at order 12 of perturbation. Similar to the procedure we envisaged in Appendix A, there is a particular configuration for the action of two-body perturbations where six $s_i^y s_j^y$ and six $s_i^x s_j^x$ act on the green and blue links of the ruby plaquette as shown in Fig. 6(a) (top). The action of V terms then projects the ground state to itself by reducing the red links of the lattice to effective vertices and encode the B_f^A plaquette operator on the logical qubits as illustrated in Fig. 6(a) (bottom). The corresponding effective operator is given by

$$B_f^{A(B)} = -(+)\prod_v \tau_v^w, \quad w = \begin{cases} x, & \text{if } v \in \mathcal{V} \\ z, & \text{if } v \in \mathcal{E} \end{cases} \quad \text{(B6)}$$

where $\mathcal{V}$ ($\mathcal{E}$) are the edges (vertices) shared by ∇_c and its surrounding $\triangle_{\bar{c}}$ ($\triangle_{\bar{\bar{c}}}$) triangles.

The last elementary IOM, B_f^B, is a closed string which appears at order 15 from the action of three $s_i^y s_j^y$ and twelve $s_i^x s_j^x$ terms, respectively on the green and blue links of the ruby plaquettes according to the convention shown in Fig. 6(b) (top). The B_f^B plaquette operator is defined in Eq. (B6) and demonstrated in Fig. 6(b) (bottom).

Defining $B_f^C = \mathcal{A}_\nabla$, it is immediately followed from the above relations that, locally, $B_f^A B_f^B = B_f^C$ and the local $\mathbb{Z}_2 \times \mathbb{Z}_2$ symmetry of the RCC model is restored in the $J_x \gg J_y, J_z$ limit. One can also check that the B_f^A and B_f^B plaquette operators can alternatively be constructed from the product of $\mathcal{A}_\nabla, \mathcal{B}_\triangle$ operators located inside B_f^A and B_f^B. The contributing $\mathcal{A}_\nabla, \mathcal{B}_\triangle$ operators in the structure of each IOM are denoted by black stars in Fig. 6.

On a triangular lattice with $N_t = N/2$ sites (N is the number of sites on the ruby lattice), there exist $N_t/3$ IOMs of each type (A, B, C) and the total number of N_t elementary IOMs. The model therefore, possesses 2^{N_t} independent IOMs.

APPENDIX C: RCC IN A MAGNETIC FIELD

In this section, we study the stability of the gapless phases in the presence of a magnetic field in the z direction, by analyzing the original RCC model (1) for $\mathbf{J}_{A_2} = (1.4, 0.4, 0.2)$ couplings. The RCC Hamiltonian in the presence of the magnetic field is given by

$$H' = -\sum_{\alpha=x,y,z} J_\alpha \sum_{\alpha-\text{links}} s_i^\alpha s_j^\alpha - h_z \sum_i s_i^z. \qquad \text{(C1)}$$

In the extreme case where $h_z = 0$, the system is in the A_2 phase, which according to our numerical results (see Sec. IV) is a gapless phase. However, in the high magnetic field limit where $J_\alpha = 0$, $(\alpha = x, y, z)$, the Pauli spins are all aligned in the field direction and the ground state of the system is given by a polarized phase in the z direction. The low-lying excitations over this polarized ground state are denoted by single spin flips each with $2h_z$ energy cost. The system is therefore gapped. When all couplings are nonzero, at least a phase transition between the A_2 gapless phase and the gapped polarized phase of the high-field limit is expected. Other intermediate phases may also emerge in between. In order to capture the possible phase transitions, we calculated the energy gap of the system as a function of h_z, as well as the ground-state energy of the system and its derivatives.

The energy gap for different values of magnetic field h_z is shown in the upper panel of Fig. 7. The results show that the A_2 gapless phase is stable up to a finite field at $h_z^{c_1} \approx 0.05$ where a phase transition occurs to an intermediate gapped phase. This latter phase is not continuously connected to a trivial polarized phase arising at high magnetic field. Indeed, a second phase transition to a polarized phase occurs at $h_z^{c_2} \approx 0.11$. In the inset of this plot we also show the SDE with respect to h_z; it clearly shows two phase transitions signaled by divergences of SDE.

The intermediate gapped phase could be a topological phase distinct from a trivial paramagnetic phase. To explore the topological properties, a natural way would be to evaluate the topological entanglement entropy of gapped phases. Given a normalized wave function $|\phi\rangle$ and a partition of the system into subsystems A and B, the reduced density matrix of subsystem A is given by $\rho_A = \text{Tr}_B |\phi\rangle\langle\phi|$. The von Neumann entropy $S = -\text{Tr}(\rho_A \log_2 \rho_A)$ measures the entanglement between two subsystems. For a two-dimensional topologically ordered gapped phase, the latter quantity assumes an area law scaling as $S = \alpha L - \gamma + O(1/L)$ [43,44], where L is the length of the region A with smooth boundary. In this expression the first term arises from the nonuniversal and local contribution of the entanglement entropy. The second term γ, however, is a universal constant being a signature of a topologically ordered phase. A distinctive feature of a topological phase is signaled by nonzero γ. We evaluated γ as a function of magnetic field h_z for gapped phases. The results are shown in the lower panel in Fig. 7. It shows that the TEE is nonzero in the intermediate gapped phase and drops to zero at the phase transition to the trivial polarized phase.

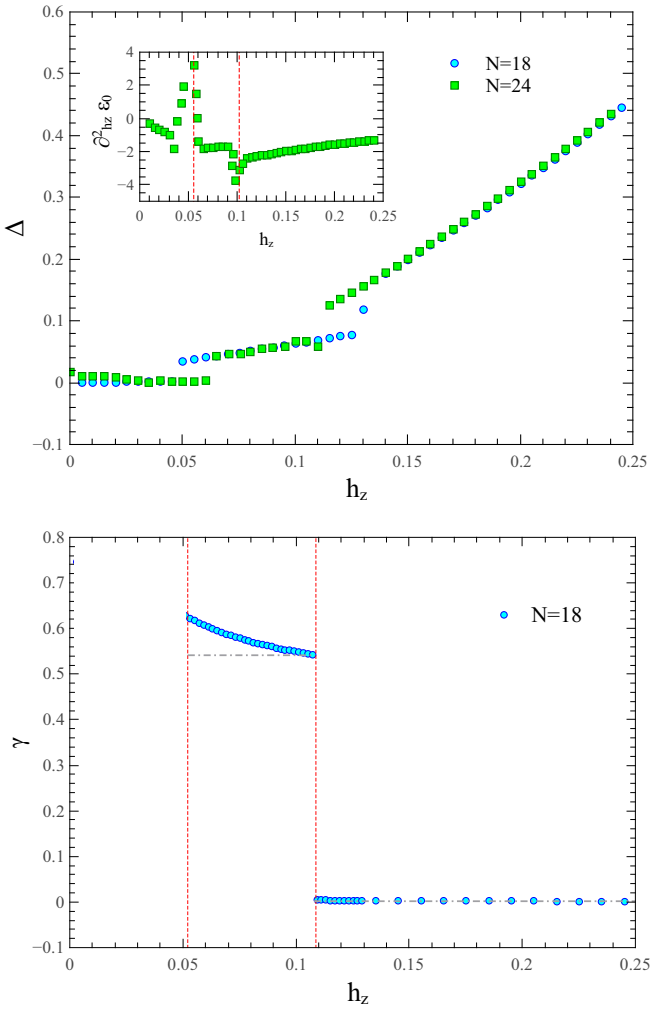

FIG. 7. Upper panel: Energy gap of Hamiltonian (1) as a function of magnetic field in the z direction obtained from ED on the ruby clusters with 18, 24 sites. The inset demonstrates the second derivative of ground-state energy with respect to h_z. The red dashed lines in the inset further demonstrate the location of the transition points. Lower panel: Topological entanglement entropy (TEE) calculated for gapped phases. TEE drops to zero at $h_z \approx 0.11$ where a phase transition between a topological phase and a trivial polarized phase occurs.

Let us note that the determined phase boundary suffers from the finite-size effects and more accurate results might be obtained by performing the calculations on larger lattice sizes using more powerful numerical arsenals. However, the nonzero TEE for small magnetic fields and its transition to zero TEE for $h_z > 0.11$ is a clear signature of two topologically distinct phases.

[1] A. Yu. Kitaev, Ann. Phys. **303**, 2 (2003).
[2] X. Chen, Z. C. Gu, and X. G. Wen, Phys. Rev. B **82**, 155138 (2010).
[3] D. C. Tsui, H. L. Stormer, and A. C. Gossard, Phys. Rev. Lett. **48**, 1559 (1982); Luc Vinet and A. Zheda, J. Phys. A: Math. Theor. **44**, 085201 (2011).

[4] X.-G. Wen, Adv. Phys. **44**, 405 (1995).
[5] X. G. Wen and Q. Niu, Phys. Rev. B **41**, 9377 (1990).
[6] X. G. Wen, *Quantum Field Theory of Many-Body Systems: From the Origin of Sound to an Origin of Light and Electrons* (Oxford University, New York, 2010), pp. 1–520.
[7] A. Kitaev, Ann. Phys. **321**, 2 (2006).
[8] C. Nayak, S. H. Simon, A. Stern, M. Freedman, and S. Das Sarma, Rev. Mod. Phys. **80**, 1083 (2008).
[9] Y. Singh and P. Gegenwart, Phys. Rev. B **82**, 064412 (2010).
[10] J. Reuther, R. Thomale, and S. Trebst, Phys. Rev. B **84**, 100406(R) (2011).
[11] Y. Singh, S. Manni, J. Reuther, T. Berlijn, R. Thomale, W. Ku, S. Trebst, and P. Gegenwart, Phys. Rev. Lett. **108**, 127203 (2012).
[12] S. K. Choi, R. Coldea, A. N. Kolmogorov, T. Lancaster, I. I. Mazin, S. J. Blundell, P. G. Radaelli, Y. Singh, P. Gegenwart, K. R. Choi, S. W. Cheong, P. J. Baker, C. Stock, and J. Taylor, Phys. Rev. Lett. **108**, 127204 (2012).
[13] A. Banerjee, C. A. Bridges, J.-Q. Yan, A. A. Aczel, L. Li, M. B. Stone, G. E. Granroth, M. D. Lumsden, Y. Yiu, J. Knolle, S. Bhattacharjee, D. L. Kovrizhin, R. Moessner, D. A. Tennant, D. G. Mandrus, and S. E. Nagler, Nat. Mater. **15**, 733 (2016).
[14] H. Yao and S. A. Kivelson, Phys. Rev. Lett. **99**, 247203 (2007).
[15] M. Kargarian, A. Langari, and G. A. Fiete, Phys. Rev. B **86**, 205124 (2012).
[16] I. Rousochatzakis, U. K. Rössler, J. van den Brink, and M. Daghofer, Phys. Rev. B **93**, 104417 (2016).
[17] V. Karimipour, Phys. Rev. B **79**, 214435 (2009).
[18] A. Langari, A. Mohammad-Aghaei, and R. Haghshenas, Phys. Rev. B **91**, 024415 (2015).
[19] H. Bombin, M. Kargarian, and M. A. Martin-Delgado, Phys. Rev. B **80**, 075111 (2009).
[20] M. Kargarian, H. Bombin, and M. A. Martin-Delgado, New J. Phys. **12**, 025018 (2010).
[21] B. Rasche, A. Isaeva, M. Ruck, S. Borisenko, V. Zabolotnyy, B. Büchner, K. Koepernik, C. Ortix, M. Richter, and J. van den Brink, Nat. Mater. **12**, 422 (2013).
[22] C. Pauly, B. Rasche, K. Koepernik, M. Liebmann, M. Pratzer, M. Richter, J. Kellner, M. Eschbach, B. Kaufmann, L. Plucinski, C. M. Schneider, M. Ruck, J. van den Brink, and M. Morgenstern, Nat. Phys. **11**, 338 (2015).
[23] C. Pauly, B. Rasche, K. Koepernik, M. Richter, S. Borisenko, M. Liebmann, M. Ruck, J. van den Brink, and M. Morgenstern, ACS Nano **10**, 3995 (2016).
[24] G. Jackeli and G. Khaliullin, Phys. Rev. Lett. **102**, 017205 (2009).
[25] H. Bombin and M. A. Martin-Delgado, Phys. Rev. Lett. **97**, 180501 (2006).
[26] D. Nigg, M. Müller, E. A. Martinez, P. Schindler, M. Hennrich, T. Monz, M. A. Martin-Delgado, and R. Blatt, Science **345**, 302 (2014).
[27] H. G. Katzgraber, H. Bombin, and M. A. Martin-Delgado, Phys. Rev. Lett. **103**, 090501 (2009).
[28] S. S. Jahromi, M. Kargarian, S. F. Masoudi, and K. P. Schmidt, Phys. Rev. B **87**, 094413 (2013).
[29] S. S. Jahromi, S. F. Masoudi, M. Kargarian, and K. P. Schmidt, Phys. Rev. B **88**, 214411 (2013).
[30] S. Capponi, S. S. Jahromi, F. Alet, and K. P. Schmidt, Phys. Rev. E **89**, 062136 (2014).
[31] M. Kargarian, Phys. Rev. A **78**, 062312 (2008).
[32] S. S. Jahromi and A. Langari, arXiv:1512.00756.
[33] J. Vidal, K. P. Schmidt, and S. Dusuel, Phys. Rev. B **78**, 245121 (2008).
[34] S. Dusuel, K. P. Schmidt, J. Vidal, and R. L. Zaffino, Phys. Rev. B **78**, 125102 (2008).
[35] J. R. Wootton, V. Lahtinen, Z. Wang, and J. K. Pachos, Phys. Rev. B. **78**, 161102(R) (2008).
[36] H. Bombin, Phys. Rev. Lett. **105**, 030403 (2010).
[37] A. Kubica, B. Yoshida, and F. Pastawski, New J. Phys. **17**, 083026 (2015).
[38] H. Bombin, G. Duclos-Cianci, and D. Poulin, New J. Phys. **14**, 073048 (2012).
[39] H. Bombín, Commun. Math. Phys. **327**, 387 (2014).
[40] A. Vaezi and M. Barkeshli, Phys. Rev. Lett. **113**, 236804 (2014).
[41] A. Vaezi, Phys. Rev. X **4**, 031009 (2014).
[42] D. L. Bergman, R. Shindou, G. A. Fiete, and L. Balents, Phys. Rev. B **75**, 094403 (2007).
[43] A. Kitaev and J. Preskill, Phys. Rev. Lett. **96**, 110404 (2006).
[44] M. Levin and X. G. Wen, Phys. Rev. Lett. **96**, 110405 (2006).